1 **Title:**

2 Mechanical heterogeneity and roles of parallel microtubule arrays in governing meiotic spindle

3 length

4

5 **Authors:**

6 Jun Takagi[1] and Yuta Shimamoto[1,2,*]

7

8 **Affiliations:**

9 [1]Center for Frontier Research, National Institute of Genetics, Yata 1111, Mishima, Shizuoka 411-

10 8540, Japan

11 [2]Department of Genetics, School of Life Science, SOKENDAI University, Yata 1111, Mishima,

12 Shizuoka 411-8540, Japan

13

14 [*]Correspondence should be addressed to Y.S. (e-mail: yuta.shimamoto@nig.ac.jp)

15 **Abstract**

16 Metaphase spindles are arrays of microtubules whose architecture provides the mechanism for

17 regulated force generation required for proper segregation of chromosomes during cell division.

18 Whereas long-standing models are based on continuous antiparallel microtubule arrays

19 connecting two spindle poles and overlapping at the equator, spindles typically possess a more

20 complex architecture with randomly arranged short filaments. How these heterogeneous

21 multifilament arrays generate and respond to forces has been mysterious, as it has not been

22 possible to directly measure and perturb spindle force while observing relevant filament motility.

23 Here, we combined microneedle-based quantitative micromanipulation with high-resolution

24 microtubule tracking of *Xenopus* egg extract spindles to simultaneously examine the force and

25 individual filament motility *in situ.* We found that the microtubule arrays at the middle of the

26 spindle half are considerably weak and fluid-like, being more adaptable to perturbing forces as

27 compared to those near the pole and the equator. We also found that a force altering spindle

28 length induces filament translocation nearer the spindle pole, where parallel microtubules

29 predominate, while maintaining equatorial antiparallel filaments. Molecular perturbations

30 suggested that the distinct mechanical heterogeneity of the spindle emerges from activities of

31 kinesin-5 and dynein, two key spindle motor proteins. Together, our data establish a link between

32 spindle architecture and mechanics, and highlight the importance of parallel microtubule arrays

33 in maintaining its structural and functional stability.

2

34   **Main Text:**

35   **Introduction**

36   Spindles are microtubule-based bipolar structures assembled to segregate chromosomes during

37   cell division. Errors in chromosome segregation are linked to aneuploidy, the hallmark of cancer

38   and several developmental disorders in humans (Gordon et al., 2012; Hassold and Hunt, 2001).

39   Forces exerted by the spindle are essential, as they pull chromosomes, monitor erroneous

40   attachment, and control spindle position in a cell (Dumont and Mitchison, 2009b; Inoue and

41   Salmon, 1995). The forces generated in turn act on the spindle and influence its length and

42   bipolarity, which ensure the distance over and axis along which chromosomes are segregated.

43   Therefore, the structure must properly respond to these forces and maintain overall integrity.

44

45   Understanding the spindle mechanics requires knowing the internal filament architecture and

46   dynamics, as well as how the arrays of the filaments generate and respond to force. In long-

47   standing models, spindles are described as arrays of long, continuous microtubules radially

48   growing from the opposite spindle poles and forming an antiparallel overlap at the equator

49   (McIntosh et al., 1969; Mitchison and Salmon, 2001; Scholey et al., 2003). Although this

50   relatively simple architecture has been widely observed in small spindles, such as those of yeast

51   (Winey et al., 1995), studies of higher eukaryote spindles, including those of *Caenorhabditis*

52   *elegans*, *Xenopus laevis*, and humans, revealed that the filament architecture in these species is

53   much more complex. In particular, the minus-ends of many microtubules are not anchored to

54   spindle poles but instead broadly distributed across the bipolar structure (Burbank et al., 2006;

55   Mastronarde et al., 1993; Redemann et al., 2017). These individual filaments are short and span

56   only part of the spindle, overlapping with each other to form a "tiled-array"-like arrangement

3

57   (Brugues et al., 2012; Yang et al., 2007). Within this architecture, individual microtubules grow

58   toward either the left or the right spindle pole (Brugues et al., 2012), forming antiparallel as well

59   as parallel filament arrays at varying spindle location. Thus, spindles are architecturally

60   heterogeneous, in terms of filament position and relative filament polarity.

61

62   Consistent with this, the poleward flux – the persistent translocation of microtubule lattices

63   characteristic of many metazoans (Ganem and Compton, 2006) – exhibits a non-uniform velocity

64   distribution along the length of the spindle. In particular, the flux speed is substantially faster

65   around the equator (~2-3 µm/min) than nearer the pole (~1 µm/min), which cannot be simply

66   expected from continuous filament lattices spanning from the pole toward past the equator

67   (Burbank et al., 2007; Yang et al., 2008). The poleward movement occurs with filament minus-

68   ends leading (Mitchison, 2005). The dynamics is linked to activities of kinesin-5 and dynein, two

69   key microtubule motors of opposite directionality. *In vitro*, kinesin-5 forms cross-bridges along

70   overlapping microtubules and pushes apart antiparallel filaments (Kapitein et al., 2005). On the

71   other hand, dynein is located at the filament minus-end and may counteract this motion (Tan et

72   al., 2018).

73

74   Despite the wealth of information on filament architecture and dynamics, the forces in the

75   spindle are poorly understood. This is because earlier studies have analyzed filament features in a

76   static sample setting, such as one required in electron microscopy, or examined the dynamic

77   samples using live cell methods, but without measuring force. Since Bruce Nicklas' seminal

78   work (Nicklas, 1997), physical manipulation studies have directly examined spindle forces in

79   cells (Garzon-Coral et al., 2016; Hiramoto and Nakano, 1988; Skibbens and Salmon, 1997);

4

80 however, the assays used in these studies employed a cell membrane that is robust against

81 physical perturbation and are thus incompatible with molecular tools, or did not accommodate

82 for single filament visualization. Hence, there is little quantitative information on the relationship

83 between spindle force and its architectural dynamics, and thus, the micromechanics of this

84 heterogeneously arranged filament assembly remain mysterious.

85

86 Here, to fill this knowledge gap, we combined microneedle-based quantitative

87 micromanipulation with fluorescence speckle microscopy to measure and perturb local spindle

88 force and to simultaneously observe individual microtubule motility *in situ*. The use of *Xenopus*

89 egg extract, which is widely used for studying many cell-cycle events including spindle assembly

90 (Hannak and Heald, 2006), allowed us to perform controlled force perturbation as well as

91 titration over labeled tubulins to achieve conditions necessary for single-filament tracking. We

92 show how the heterogeneously arranged microtubule arrays respond to force and slide apart

93 while maintaining overall stability, and its dependency on motor protein activities.

94

95 **Results**

96 ***Establishing a method for probing local mechanical responses of microtubules in the***

97 ***metaphase spindle***

98 We used force-calibrated microneedles (stiffness: 0.3–0.5 nN/µm) to probe mechanical responses

99 of microtubules that assemble the *Xenopus* metaphase spindle (Fig. 1A). The microneedles had

100 sufficient bending flexibility and axial rigidity, enabling us to insert the probe tip into the dense

101 microtubule arrays while applying calibrated local force along the pole-to-pole axis of the

102 spindle, the direction along which microtubules roughly align and slide apart. The magnitude of

103   the force applied ranged from 0.4 nN to 1.1 nN, the amount typical for chromosome pulling and

104   spindle positioning in a cell (Garzon-Coral et al., 2016; Zhang and Nicklas, 1999). Microtubule

105   motion response was simultaneously observed using spinning-disk confocal microscope, by

106   tracking the fluorescent 'speckles' from X-rhodamine-labeled tubulins (20 nM) incorporated into

107   the filament lattices (probability: <0.4 per filament) (Yang et al., 2007) (Fig. 1B). Images were

108   acquired at ~5 µm above the coverslip surface, a distance that allowed minimal surface friction

109   but sufficient imaging sensitivity.

110

111   Under these conditions and in the absence of an external force, tubulin speckles exhibited

112   persistent poleward translocation at ~2–3 µm/min, while exhibiting stochastic motion fluctuation

113   along the filament's long axis, in agreeing with previous reports (Yang et al., 2007) (Fig. 1C, D).

114   To determine the mechanical responses of individual microtubules, we needed to eliminate this

115   intrinsic motion 'noise'. To this end, we developed a method based on oscillatory force input. As

116   shown in Fig. 1E and F, the application of a sinusoidal force at an optimized frequency (0.1 Hz)

117   resulted in periodic back-and-forth movements in the majority of tubulin speckles (>80% of

118   total) without perturbing the overall flux dynamics. The amplitude of the induced speckle

119   movement, which appeared predominantly along the spindle's pole-to-pole axis (Fig. S1A), was

120   determined based on a least-square fitting to a sinusoidal function (Fig. S1B) and then mapped

121   onto a two-dimensional heat map (Fig. 1G). Projecting the heat map onto the long (Fig. 1H) and

122   short (Fig. 1I) spindle axes revealed the extent of induced speckle movement and its spatial

123   dependency. The speckles' oscillatory responses did not decay over time (Fig. S1C), provided

124   that our measurements were made while the steady-state metaphase structure was maintained.

125   Further, as the flux dynamics persisted, the direction of the time-averaged speckle movement

6

126   could be used to define filament polarity. We thus established a method for analyzing local force

127   responses of spindle microtubules depending on filament position and polarity.

128

129   ***Microtubule arrays at the middle of the spindle half are more mechanically compliant than***

130   ***those near the pole and the equator***

131   Using this approach, we first asked whether the mechanical responses of microtubules differ

132   depending on their position in the spindle (Fig. 2). The microneedle tip was inserted into either

133   of three spindle regions: near the pole, near the equator, or at the middle of the spindle half.

134   Speckle motion amplitude profiles (as in Fig. 1G) were obtained for multiple spindle samples,

135   pooled, and averaged to generate an average motion amplitude profile along the long (Fig. 2A–

136   C) and short (Fig. 2E–G) spindle axes. We found that for forces applied near the spindle pole (<5

137   µm from the structure's edge), the profile showed a plateau phase over ±5 µm from the point of

138   force application (<10 % drop), indicating a coupled lattice movement at the vicinity of the

139   spindle pole (Fig. 2A). This concerted lattice movement was also observed when force was

140   applied near the spindle equator (<5 µm from the structure's center), albeit that the amplitude

141   was maintained toward both spindle poles (Fig. 2C). Notably, however, when force was applied

142   at the middle of the spindle half (i.e. between the pole and the equatorial regions), we observed

143   much steeper amplitude decay (>50% drop) within the same ±5-µm distance (Fig. 2B).

144   Normalized motion amplitude profiles further revealed that the induced relative lattice

145   movement was >2-fold larger at the middle of the spindle half (slope: 0.13 ± 0.05) than near the

146   pole (0.03 ± 0.02) and the equator (0.06 ± 0.05) (n = 5 each, Fig. 2D). Speckles located along the

147   short spindle axis also exhibited substantial movement parallel to the direction of force

148   application (Fig. 2E–H), indicating lateral mechanical coupling between neighboring filaments.

149 Therefore, the arrays of microtubules are mechanically coupled in both longitudinal and lateral

150 directions, and the coupling strength varies depending on spindle location.

151

152 Based on the extent of local lattice movement and the amount of force applied, we estimated the

153 dynamic modulus of the spindle, a measure of the structure's stiffness (see Materials and

154 Methods). The moduli for the long axis were 5.6 ± 2.0, 1.4 ± 0.2, and 3.2 ± 1.4 kPa (or $\times 10^3$

155 $pN/\mu m^2$) at the pole, the middle of the spindle half, and the equator, respectively (magenta, Fig.

156 2I) (n = 5). On the other hand, the moduli for the short axis were much smaller overall, but also

157 depended on spindle location: 0.7 ± 0.3, 0.3 ± 0.1, and 0.4 ± 0.2 kPa, in the same location order

158 (cyan, Fig. 2I). The values are in an order of magnitude comparable to previously measured

159 macroscopic spindle stiffness (several kPa) (Itabashi et al., 2009; Takagi et al., 2014) and

160 indicate the substantial local mechanical compliance of filament arrays at the middle of the

161 spindle half.

162

163 Our previous study showed that the spindle is a viscoelastic material (Shimamoto et al., 2011),

164 and thus, the local mechanical responses may vary depending on the timescale at which forces

165 are applied. As our method allowed for analyzing speckle motion at relatively slow timescales

166 (e.g. 0.1 Hz), we conducted an independent stiffness measurement based on microrheology

167 analysis (Fig. S2A–D). The analysis revealed greater mechanical compliance at the middle of the

168 spindle half than near the pole and the equator, over a range of timescales from minutes to sub-

169 seconds (frequency: 0.02–4 Hz) (Fig. 2J). Moreover, the structure underwent a predominantly

170 viscous, fluid-like deformation at the middle of the spindle half, whereas the structure close to

171 the spindle pole exhibited less fluidity (Fig. 2K). Together, microtubule arrays at the middle of

172   the spindle half engage in a relatively weak, viscous mechanical coupling, whereas those around

173   the spindle pole are more rigid and elastic.

174

175   ***Spindle microtubule response to force is independent of filament polarity***

176   Microtubules in the spindle orient toward either the left or the right spindle pole, and the

177   proportion varies depending on their location in the spindle. To test whether this filament feature

178   leads to different mechanical outputs, we analyzed the dependency of the speckles' force

179   responses on filament polarity (Fig. 3). Tubulin speckles were classified into two groups based

180   on the directionality of their persistent poleward movements, and then the force-induced motion

181   amplitude was determined as described above (Fig. 3A). Consistent with previous studies, the

182   two motile fractions appeared nearly equal at the equator (~50:50), while those moving toward

183   the proximal spindle pole became predominant nearer the pole (~80:20), suggesting the

184   predominance of parallel filaments with their minus-ends facing outward (n = 4, Fig. 3B).

185   However, we found no significant differences in speckle motion amplitude depending on the

186   assigned filament polarity, within the accuracy that could resolve its regional variation (Fig. 3C).

187   The analysis was conducted for multiple spindle samples (n = 4), with consistent results (Fig.

188   3D). These findings suggest that at each spindle location, microtubules engage in approximately

189   equal mechanical coupling regardless of filament orientation. In addition, the compliant filament

190   array at the middle of the spindle half is predominantly parallel.

191

192   ***Microtubule arrays nearer the spindle pole predominantly slide outward against pole-***

193   ***separating force while the dynamics of equatorial filaments are maintained***

194   The local microtubule responses we characterized thus far occurred at sub-micron length scale,

195   while spindles maintained a steady pole-to-pole length. To examine how the filaments respond to

196   force that influences macroscopic spindle-length, we employed a dual-microneedle setup (Takagi

197   et al., 2014) and induced a global length perturbation of the spindle (~20% increase from the

198   steady-state size) (Fig. 4A). Spindles were double-labeled with Alexa 488-tubulin (400 nM) and

199   X-rhodamine-tubulin (20 nM) for imaging their overall morphology and individual microtubule

200   motion dynamics, respectively, and were stretched by moving one microneedle away from the

201   other (Fig. 4B). The stretching speed (100 nm/s) was such that it led to the development of nN-

202   order force across the length of the bipolar structure (Takagi et al., 2014). The analysis was

203   conducted for speckles that could be tracked for >10 s, a period that covers average tubulin

204   turnover in spindles (~30–60 s) (Needleman et al., 2010; Salmon et al., 1984). As shown in the

205   kymograph (Fig. 4C), soon after the microneedle movement was initiated ($t = 0$), the spindle first

206   underwent a brief period of parallel translocation due to mechanical compliance between the

207   probe tip and the spindle (labeled "Trans" in Fig. 4C), and then continuously elongated until the

208   microneedle motion was stopped (labeled "Stretch" in Fig. 4C). Quantitative analysis revealed

209   that during the course of the stretch, spindle length increased at a nearly constant velocity (96 ±

210   26 nm/s, n = 4) and reached ~110–130% of the initial pole-to-pole distance (34.2 ± 6.0 µm to

211   40.7 ± 6.2 µm, n = 4) (orange highlighted area in Fig. 4D). Associated with this change, tubulin

212   speckles moved predominantly parallel to the force application direction and yielded trajectories

213   of various contour lengths (Fig. 4E). Average instantaneous velocities of the speckles were

214   calculated along individual trajectories and then corrected for velocities relative to the spindle

215   center to compensate overall bias toward the moving spindle pole.

216

10

217   In the absence of an external force, we observed that the speckles exhibited a non-uniform

218   velocity distribution along the long spindle axis (Fig. 4F, G), consistent with previous reports

219   (Burbank et al., 2007; Yang et al., 2008). The average absolute velocity was 2.4 ± 1.3 µm/min

220   around the equator (n = 135 tracks; blue highlighted area, Fig. 4G) and 1.4 ± 1.0 µm/min nearer

221   the pole (n = 63 tracks; white area, Fig. 4G). When the outward stretching force was applied (Fig.

222   4H, I), the speed of speckle movement nearer the spindle pole increased to a level that nearly

223   matched the rate of spindle elongation (2.3 ± 1.4 µm/min; n = 33 tracks) (white area, Fig. 4I).

224   Notably, however, this force did not significantly influence the dynamics of speckles located

225   around the equator, where the bidirectional antiparallel movement was maintained at nearly the

226   intrinsic velocity (2.4 ± 1.2 µm/min; n = 93 tracks, blue highlighted area in Fig. 4I). During the

227   course of the stretch, the overall distribution of speckle velocity maintained symmetry, indicating

228   that the manipulation was applied evenly (histograms in Fig. 4G, I). We repeated the analysis for

229   three additional spindles that had been successfully stretched, and consistently observed the

230   preferential acceleration of speckle translocation nearer the pole versus the equator (Fig. S3A).

231   The enhanced speckle motility was most likely caused by induced relative filament sliding, not

232   breakage of the filaments, because a majority of speckles maintained steady translocation speed

233   during the course of stretch (Fig. S3B). Further, the magnitude of the force applied (<1 kPa) was

234   orders of magnitude lower than the tensile strength of microtubules (>1 MPa) (Peter and Mofrad,

235   2012).

236

237   Fig. 4J summarizes the effect of an applied stretching force on the speed of speckle movement at

238   various spindle locations. The profile should yield a straight line if the change in speckle

239   movement is uniform across the spindle length (grey broken line in Fig. 4J; for schematic, see

240   Fig. 4K). On the other hand, the profile deviates from the linear relationship when predominant

241   sliding occurs nearer the pole or the equator (solid and dotted lines, respectively, in Fig. 4J; Fig.

242   S3C). Our data is more consistent with a concave shape, indicating that major filament sliding

243   took place nearer the pole, including the middle of the spindle half (red plots in Fig. 4J). Together,

244   the microtubule arrays nearer the spindle pole adapt to a force that perturbs the spindle's pole-to-

245   pole distance, while the dynamics of equatorial filament arrays are largely unperturbed.

246

247   ***Kinesin-5 contributes to the rigidity of microtubule arrays near the pole and the equator***

248   To explore the molecular mechanisms underlying the local microtubule responses, we

249   molecularly perturbed the key spindle motors, kinesin-5 and dynein (Fig. 5). The single

250   microneedle setup was used for these analyses as it enabled us to measure the mechanics of

251   essentially any spindle phenotype, including spindles with fragile poles. Our primary focus was

252   on kinesin-5, which localizes all along the spindle and is enriched near the pole (Sawin et al.,

253   1992). We first used AMPPNP (1.5 mM), a slow-hydrolyzing ATP analogue that immobilizes

254   kinesin-5 onto the microtubule lattice in the "rigor" state (Kapoor and Mitchison, 2001). Dynein

255   is relatively insensitive to AMPPNP (Heald et al., 1996). This treatment did not significantly

256   alter overall spindle length and bipolarity (Fig. 5A); however, we found a global reduction in

257   mechanical responses of the microtubule arrays across the length of the bipolar structure (Fig.

258   5B–D, Fig. S4A). The local dynamic modulus (stiffness) increased accordingly (11.7 ± 2.7, $3.5 \pm$

259   1.6, and 4.0 ± 1.6 kPa at the pole, middle, and equator; $n = 3$ each), with statistical significance at

260   the pole and the middle of the spindle half (Fig. 5E), suggesting that persistent cross-bridges

261   were made between overlapping microtubules.

262

12

263   Next, we used monastrol, an inhibitor of kinesin-5. Monastrol reduces the affinity of kinesin-5

264   for the microtubule lattice *in* vitro (Kwok et al., 2006). Although spindles collapsed at a high

265   dose (e.g. 100 µM), bipolarity was maintained when using a relatively low dose (i.e. 10 µM), the

266   efficacy of which was confirmed by the reduced flux velocity (1.0 ± 0.1 µm/min, n = 5; versus

267   1.7 ± 0.3 µm/min for control, n = 7) (Fig. S4B, C). We found that upon this treatment, the

268   speckle motion profile obtained nearer the spindle pole were similar or slightly suppressed as

269   compared to control (orange in Fig. 5G, H). On the other hand, the profile exhibited a sharper

270   amplitude peak for forces applied near the spindle equator, suggesting enhanced relative filament

271   movement (orange in Fig. 5I). When we increased the monastrol dosage (i.e. 20 µM), spindles

272   shortened to 26.1 ± 4.2 µm (n = 6; versus 37.4 ± 4.8 µm for control) while still maintaining

273   steady length and bipolarity (Fig. S4B, D). Although such small spindles could be analyzed only

274   at two regions, the profiles became much sharper both at the pole and at the equator (red in Fig.

275   5G, I; Fig. S4E). The estimated local dynamic moduli indicated that the equatorial filament

276   arrays are sensitive to kinesin-5 inhibition, acquiring ~3-fold mechanical compliance upon

277   monastrol treatment (1.4 ± 0.8 kPa at 10 µM; 2.1 ± 0.5 kPa at 20 µM, n = 3 each) (Fig. 5J). The

278   filament array near the spindle pole was less sensitive to this inhibition, but also became

279   compliant upon increasing the dosage (7.5 ± 2.3 kPa at 10 µM; 3.3 ± 1.4 kPa at 20 µM; n = 3 and

280   5, respectively) (Fig. 5J). Together, these data suggest a broad localization of kinesin-5 across the

281   bipolar structure, and that the activity is required for maintaining spindle length while achieving

282   robust filament couplings near the pole and the equator.

283

284   ***Dynein contributes to the coupling of microtubule arrays away from the equator***

13

285   We next focused on dynein, a minus-end directed microtubule motor whose well-characterized

286   function is spindle pole organization (Compton, 1998). An addition of the monoclonal antibody

287   to the dynein light chain (Gaglio et al., 1997) resulted in a barrel-like microtubule array with

288   sprayed poles, the common phenotype of dynein inhibition (Fig. 5K). Because of the unfocused

289   pole, the spindle regions were defined based on the distance solely from the equator such that it

290   nearly matches the region classification of unperturbed spindles (white dotted lines, Fig. 5K).

291   Upon dynein inhibition, we found a noticeable sharpening of the motion amplitude profile at >15

292   µm away from the equator (Fig. 5L and S4F), consistent with sparse microtubule arrays seen in

293   fluorescence images. Importantly, the difference was also observed at 5-15 µm regions from the

294   equator (Fig. 5M), but was not prominent nearer the equator (<5 µm region) (Fig. 5N). The local

295   stiffness moduli estimated were 1.2 ± 1.5, 0.8 ± 0.3, and 2.6 ± 1.0 kPa (n = 4 each) for regions <5

296   µm, 5–15 µm, and >15 µm from the equator, among which ≥5 µm regions yielded statistically

297   significant weakening of the structure as compared to control (Fig. 5O). These suggest that

298   dynein contributes to the mechanical coupling of microtubule arrays all along the spindle, except

299   for those around the equator.

300

301   **Discussion**

302   Our microneedle-based quantitative micromanipulation with high-resolution fluorescence

303   imaging enabled for directly probing the dynamic changes in position and motility of

304   microtubules in the spindle that respond to applied forces. We found that microtubules at the

305   middle of the spindle half engage in less rigid, more fluid-like mechanical coupling with

306   neighboring filaments and exhibit larger relative movement against perturbing forces, as

307   compared to those around the spindle pole and the equator. Consistent herewith, we discovered

14

308   that microtubule lattices nearer the spindle pole are extensively slid apart from the equator in

309   response to force altering the pole-to-pole distance, while the arrays of equatorial antiparallel

310   filaments were maintained. From these findings, we propose a model of spindle micromechanics,

311   which is determined by mechanically robust microtubule arrays at the pole and the equator, and

312   more loosely coupled filament arrays at the middle of the spindle half (Fig. 6A).

313

314   Currently, the most advanced models of metazoan spindles describe a steady-state spindle

315   architecture assembled from the collection of short microtubule filaments (Brugues et al., 2012;

316   Burbank et al., 2007; Yang et al., 2008; Yang et al., 2007); however, none explicitly explains the

317   physical nature of the filament interactions and how forces influence their arrangement and

318   motility. . By mechanically perturbing the spindle, we found that there is a predominant fraction

319   of equatorial microtubules whose mechanical coupling to the spindle pole is considerably weak,

320   and thus, their dynamics is insensitive to a force that pulls the two poles apart. On the other hand,

321   microtubule arrays nearer the spindle pole engage in more rigid mechanical connection and their

322   movement is tightly coupled to spindle-length change. Given the shortness of the filaments, the

323   microtubule array at the middle of each spindle half is likely formed by overlapping ends of

324   equatorial antiparallel filaments and polar parallel filaments (blue highlighted area in Fig. 6A).

325   Our data show that this predominantly parallel filaments array has less mechanical resistance

326   than other spindle location and can adapt to force that alters the pole-to-pole distance. Further,

327   microtubules growing from the opposite spindle pole engage in nearly equivalent mechanical

328   coupling with neighboring filaments, masking their structural polarity. These filament-coupling

329   features, which are relatively weak, spatially heterogeneous, and polarity-independent, enable the

330   spindle to transmit and respond to force in a manner that is distinct from the long-standing model

15

331   of spindle assembly, in which the arrays of equatorial antiparallel microtubules connect two

332   spindle poles and balance the pole-to-pole distance (Inoue and Salmon, 1995; Mitchison and

333   Salmon, 2001; Scholey et al., 2003).

334

335   Our results also suggest how the robust and adaptable nature of the microtubule arrays emerges

336   from motor protein mechanics. At the spindle equator, the major protein that maintains the

337   filament dynamics is likely kinesin-5, as our data showed the sensitivity of the equatorial

338   mechanics to chemical inhibitor. When kinesin-5 was inhibited, filament sliding slowed down,

339   most likely because of a lower number of force generators acting against a constant load, and

340   further, the filaments more easily slid apart against the force perturbing their motility. Unlike

341   other kinesins, such as vesicle transporting kinesin-1, *Xenopus* kinesin-5 can maintain a stable

342   association with the lattices of microtubules and generate substantial braking force against fast

343   filament sliding (Shimamoto et al., 2015; Valentine et al., 2006). This resistive motor force is

344   additive (Shimamoto et al., 2015) and can thus accumulate across the filament overlap of several

345   microns at which many kinesin-5 molecules localize (Kashina et al., 1996). Because of these

346   motor properties, each kinesin-5 molecule should experience only a subtle force fluctuation that

347   is insufficient to perturb the intrinsic enzymatic cycle, thus maintaining the speed of antiparallel

348   filament sliding and preventing excess filament translocation against perturbing forces ("Equator"

349   in Fig. 6B). Our inhibition assays suggested that, around the spindle pole, kinesin-5 also

350   crosslinks parallel microtubules and enhances filament coupling, as predicted from its substantial

351   pole localization (Sawin et al., 1992) and reconstitution assays (Kapitein et al., 2005; Shimamoto

352   et al., 2015). Filament coupling at the pole also depended on dynein, in agreement with previous

353   studies (Gaglio et al., 1997; Tan et al., 2018). Thus, kinesin-5 and dynein may act together to

16

354   make the rigid filament coupling when microtubules reach the pole ("Pole" in Fig. 6B). In

355   contrast to these robust structures, however, those at the middle of the spindle half appeared

356   much more compliant. Our findings suggest that within this filament array where predominant

357   microtubules run in parallel, kinesin-5 crosslinking activity is largely suppressed ("Middle" in

358   Fig. 6B). On the other hand, dynein plays a prominent role, likely via its minus-end

359   accumulation and lateral interaction with adjacent filaments (Hueschen et al., 2017; Tan et al.,

360   2018) ("Middle" in Fig. 6B). Based on our measurement of local spindle stiffness (~1,000

361   pN/µm^2) and the density of microtubules (~100/µm^2), the linkage could generate ~10 pN force

362   per filament, an amount 2- to 5-fold larger than the stall force of single dynein molecules

363   walking along a single microtubule (Gennerich et al., 2007; McKenney et al., 2010; Torisawa et

364   al., 2014). The parallel filament interaction could also be mediated by non-motor microtubule-

365   associated proteins such as the augmin complex, which caps the filament minus-ends and

366   promotes microtubule branching (Goshima et al., 2008). This might be the basis of the

367   mechanical resistance that was observed upon dynein inhibition. The viscous, fluid-like property

368   identified nearer the equator reflects the dynamicity of crosslinkers that allows for filament re-

369   arrangements, whereas the elastic property nearer the pole suggests static, persistent cross-

370   bridges. Our work thus predicts a rich micromechanics underlying parallel microtubules, which

371   is less appreciated but as important as that in antiparallel filaments.

372

373   In the spindle, chromosomes are captured by another subset of parallel microtubules, called

374   kinetochore microtubules or k-fibers, which run across the spindle half and pull the chromatids

375   toward the poles. Although this filament fraction was minor in our present study (<10% of total

376   filament number), their length must also be coupled to spindle length in order to prevent

377   chromosomes from detaching. A recent electron tomography study revealed that kinetochore

378   microtubules of *C. elegans* spindles are not continuous, but rather, their minus-ends are

379   terminated midway and embedded within a network of short microtubules assembled around the

380   pole (Redemann et al., 2017). In addition to the previously identified mechanism regulating

381   filament depolymerization at the fiber ends (Dumont and Mitchison, 2009a; Skibbens and

382   Salmon, 1997), we predict that the mechanical linkage between the filaments is compliant and

383   can adapt to force. Capturing the motility of individual microtubules within this thick filament

384   bundle would be an important next challenge to build a complete model of spindle

385   micromechanics.

386

387   Our findings on spindle's mechanical heterogeneity suggest functional advantages as it allows

388   for maintaining the equatorial spindle dynamics while controlling the pole-to-pole distance. The

389   equatorial microtubule arrays serve as structural scaffolds for physical stretching of kinetochores

390   (Elting et al., 2017) and for biochemical signaling of cytokinetic furrow positioning (Oegema

391   and Mitchison, 1997). We anticipate that the mechanically distinct local microtubule arrays

392   maintain these spindle functions, ensuring the robustness of chromosome segregation while

393   adapting to perturbation for error-free cell division.

Materials and Methods

Spindle assembly

Metaphase spindles were assembled in extracts prepared from unfertilized *X. laevis* eggs according to a well-established method (Desai et al., 1999). Freshly prepared, cytostatic factor-arrested extracts (30 µl per reaction) were first supplemented with demembranated *X. laevis* sperm nuclei (400 nuclei/µl) and released into interphase by addition of Ca^{2+} at a final concentration of 0.4 mM. Following 90-min incubation at 18°C, reactions were diluted with the equal volume of fresh extracts and cycled back into metaphase. Following 50-min incubation, X-rhodamine-labeled tubulin and Alexa 488-labelled tubulin, prepared according to a previously described method (Hyman et al., 1991), were added to extracts at a final concentration of 20 nM and 800 nM, respectively. SYTOX Green (S7020, Invitrogen) was also added to extracts at a final concentration of 250 nM for chromosome imaging. Experiments were performed 60–150 min from the start of spindle assembly, during which no noticeable changes in spindle mechanics and overall morphology were observed.

Microneedles

Microneedles were prepared by pulling glass rods (G1000, Narishige) using a capillary puller (PC-10, Narishige) followed by processing of their tips using a microforge (MF-100, World Precision Instruments) (Shimamoto and Kapoor, 2012). For precise control over its position and movement in viscous egg extracts while probing spindle force with sufficient sensitivity, the tip of each force-calibrated microneedle was made ~1–2 µm in diameter and ~100–300 µm in length, which yielded a stiffness of 0.3–0.5 nN/µm as determined by the cross-calibration method (Shimamoto and Kapoor, 2012). The tips of microneedles used in spindle-stretching experiments

19

417   were made >100-times stiffer, with ~2-µm diameter and ~50-µm length.

418

419   ***Microscopy***

420   Spindle micromanipulation was carried out in an inverted light microscope (Ti-E, Nikon)

421   equipped with a pair of three-axis hydraulic micromanipulators (MHW-3, Narishige), a 100×

422   objective (Apo TIRF, 1.49NA, Nikon), an objective scanner (PIFOC, Physik Instrumente), a

423   motorized sample stage (MS-2000, Applied Scientific Instruments), a spinning-disk confocal unit

424   (CSU-X1, Yokogawa), and an sCMOS camera (Neo 4.0, Andor). Two excitation lasers (488 nm

425   and 561 nm, 40 mW, OBSI, Coherent) were merged using an in house-built laser combiner and

426   were introduced into the confocal unit via an optical fiber (Yokogawa). The microscope and

427   imaging instruments were wired to a computer and controlled using image acquisition software

428   (NIS-Elements, ver. 4.50, Nikon).

429

430   For oscillatory perturbation experiments, a single-microneedle setup was used. First, 4 µL of a

431   cycling extract containing pre-assembled spindles was placed in an open experimental chamber,

432   which was assembled from a coverslip (Matsunami) and a rubber plate with 10-mm central

433   aperture, and covered with mineral oil (M-5310, Sigma). Under a confocal microscope, a bipolar

434   spindle of typical size and shape was selected under low illumination conditions, and the tip of a

435   force-calibrated microneedle was inserted into the region of interest within the spindle. The

436   microneedle tip was brought down to 1–2 µm above the coverslip while maintaining nearly

437   vertical approaching angle (>80° with respect to the horizontal plane). The microneedle base was

438   held by a translational piezo actuator (P-841.20, Physik Instrumente) whose displacement was

439   controlled by a voltage signal generated in an in house-written LabView program (National

440 Instruments) and sent via a closed-loop piezo driver (E-665, Physik Instrumente). Experiments

441 were performed using a sinusoidal force (frequency: 0.1 Hz) applied by moving the microneedle

442 tip parallel to the spindle pole-to-pole axis. The amount of force applied was estimated based on

443 the displacement of the microneedle tip from its equilibrium position, which was determined

444 using time-lapse imaging of the tip and piezo sensor reading. Time-lapse images were acquired

445 at a single confocal plane (~5 µm from the coverslip surface) with pre-optimized image

446 acquisition settings (interval: 1 s; exposure time: 200 ms for 488 nm and 500 ms for 561 nm) that

447 fulfilled the following requirements: 1) photo-damage and photobleaching were minimal, and 2)

448 individual tubulin speckles could be tracked across the time-lapse sequence.

449

450 For microrheology analysis, a piezo-based nano-positioning stage (Nano-LP200, Mad City Lab)

451 was mounted onto the motorized sample stage and moved in a sinusoidal manner at a fixed

452 frequency (0.02–4 Hz) and amplitude (0.7–1.0 µm) along the pole-to-pole axis of the spindle.

453 The base of the force-calibrated microneedle was held at a fixed position throughout the

454 measurement while its tip was inserted into the spindle. Bright-field images were acquired at the

455 sampling rate 50-times the frequency of the oscillatory force input for measurements at ≤0.2 Hz

456 (e.g. 1,000 ms interval for 0.02 Hz input), and at a fixed 40-ms interval for measurements at >0.2

457 Hz. The magnitude of applied force was monitored based on the microneedle tip's displacement.

458 The amount of spindle deformation was estimated by the relative displacement of the

459 microneedle tip and the spindle, whose position change was monitored by tracking the center of

460 a tracer microbead (LB30, Sigma) immobilized onto the coverslip surface.

461

462 For stretching perturbation experiments, the microscope setup as described above was used, but

463   with a dual-microneedle setup (Takagi et al., 2014). In each experiment, a single bipolar spindle

464   of typical size and shape was captured by inserting the tips of the microneedles near the opposite

465   spindle poles (<5 µm from the structure's edge). One microneedle was used to pin down the

466   spindle while the other microneedle was used to stretch the bipolar structure at a constant

467   velocity (100 nm/s). The stretching motion of the microneedle was controlled by either manual

468   steering of the micromanipulator or using the piezo actuator attached to the microneedle base.

469   Time-lapse images were acquired in a single confocal plane at 3-s intervals while switching two

470   excitation lasers with <200 ms time delay (exposure time: 400 ms for 488 nm and 300 ms for

471   561 nm). Spindles displaying no visible elongation in response to the micromanipulation (<10%

472   of the original steady-state length) usually associated with pole disorganization and were

473   excluded from subsequent analyses.

474

475   ***Molecular perturbation***

476   AMPPNP (Sigma) was used at a final concentration of 1.5 mM after adjustment of the pH to

477   ~7.7 with potassium hydroxide. Monastrol (M8515, Sigma) was used at a final concentration of

478   10 or 20 µM in the presence of 0.5% DMSO. Monoclonal antibody to the dynein light chain

479   (D5167, Sigma) was first dialyzed against a buffer comprised of 50 mM potassium glutamate

480   and 0.5 mM $MgCl_2$ using a centrifugal membrane filter (Amicon Ultra, Millipore) and then

481   added to extracts at a final concentration of 1 mg/ml (Heald et al., 1997). Reagents were

482   prepared as 50–100× working stocks in CSF-XB (10 mM K-Hepes, pH 7.7, 1 mM Mg^{2+}, 1 mM

483   EGTA, 150 mM KCl, 50 mM sucrose) and were added to extracts containing pre-assembled

484   spindles.

485

486 *Data analysis*

487 Spindle length was measured on the basis of fluorescence images of Alexa 488-tubulin. In each

488 image of a time-lapse sequence, a line-scan was performed along the pole-to-pole axis of the

489 spindle. The edges of the line-scan profile were detected on the basis of an intensity threshold

490 that was set at 25% of the maximal spindle signal intensity. The distance between the two edge

491 positions was defined as the spindle length.

492

493 Speckle motion was analyzed on the basis of fluorescence images of X-rhodamine-tubulin. The

494 entire time-lapse image stack from each experiment was first low-pass filtered (pixel width: 2 ×

495 2) in the NIS-Elements software and then loaded in the Particle Track and Analysis plugin

496 (https://github.com/arayoshipta/PTA2) in ImageJ. Speckles were detected on the basis of the total

497 intensity and size of fluorescence spots that exceeded fixed threshold values, and then, their

498 intensity profiles were each fit to a two-dimensional Gaussian function for calculating the

499 centroid position. The speckles that were detected in each image were then linked across the

500 time-lapse sequence, with fixed linking parameters. After visual inspection of representative

501 speckle trajectories, the motion of each speckle was analyzed as follows:

502

503 *1) Oscillatory perturbation experiments.* The time recording of each speckle displacement

504 along the long spindle axis (x_L) was fit to a sinusoidal function, which was given by $x_L(t) = A$

505 $\sin(\omega t + \theta) + Bt + C$. Here, A is the amplitude of speckle motion, ω is the angular frequency

506 corresponding to the input force sinusoid (0.1 Hz, $\omega \sim 0.63$ rad/s), θ is the oscillatory phase,

507 and t is the time elapsed from the onset of force application. The variable B is to compensate

508 translational movements of speckles associated with the poleward flux; a plus or minus sign

23

509   was used to assign the polarity of each microtubule filament. The variable C is to correct

510   initial position offset. Fitting was conducted in Origin 2016 (Origin Lab) and data that yielded

511   an R^2 value above 0.25 were used for subsequent analyses. The profile of speckle motion

512   amplitude along the long and short spindle axes was generated on the basis of data of speckles

513   whose initial tracking point was included within a ROI. The ROI was drawn along each

514   spindle axis (width: ± 2.5 µm). After the removal of outliers (defined as speckles exceeding

515   the peak amplitude of the speckle closest to the force application point) followed by

516   smoothing of the data plots (using 5-µm moving average filter) and offset correction

517   (subtracting the translational drift of the entire structure, ~0.1 µm typical), each profile was

518   aligned at the local maximum within a ±5-µm region from the initial microneedle position,

519   and profiles were averaged over multiple spindle samples.

520

521   *2) Spindle stretching experiments.* For individual speckle trajectories acquired during the

522   steady lengthening phase (see the Results section), the instantaneous velocity of the speckle

523   was calculated by dividing the contour length of each trajectory by the period over which the

524   speckle was tracked. Speckles that could be tracked over ≥10 s (≥3 successive time-lapse

525   frames) were used for subsequent analyses. The velocity data were plotted in a single imaging

526   plane based on the position relative to the spindle equator, which was calculated using the

527   initial tracking point of each speckle and the length and width of the spindle at the

528   corresponding time point.

529

530   The magnitude of the force (F) applied was estimated on the basis of the pre-calibrated

531   microneedle tip stiffness (k_M) and its displacement from the equilibrium position (Δx_M) according

24

532   to Hooke's law, which is given by $F = k_M \, \Delta x_M$.

534   For microrheology analysis, time-dependent changes of the force and spindle deformation were

535   each fit to a sinusoidal function, which was given by $A(t) = A_0 \sin(\omega t + \theta)$, and used to

536   determine the amplitude and phase. The effective stiffness was determined by the ratio of the

537   force to the deformation amplitude. The phase shift was determined by the difference between

538   the two oscillatory phases.

540   Local spindle region (i.e. pole, equator, and middle) was classified on the basis of the distance

541   from either the structure's center or its outer edge, measured along the pole-to-pole axis of the

542   spindle. The pole region was defined as the area within 5 µm from the structure's outer edge. The

543   equator region was defined as the area within 5 µm from the structure's center. The middle

544   region was defined as the area between the two above regions. Based on these definitions,

545   reduced-sized spindles at 20 µM monastrol allowed for data acquisition at only the equatorial

546   and pole regions. For spindles with dynein inhibition, the regions were defined solely on the

547   basis of the distance from the structure's center (<5 µm, 5–15 µm, and >15 µm) because of

548   defocused spindle poles.

550   The dynamic modulus of the spindle was estimated as follows. First, we measured local

551   deformation of microtubule arrays that developed within a 5 × 5-µm area around the point of

552   force application, analyzed on the basis of relative speckle movement in the x-y plane (i.e. the

553   imaging plane; x, long spindle axis; y, short spindle axis) and assuming that the deformation was

554   even across the z-axis (i.e. over the entire spindle width). Below, we use the following indices for

25

555　　each coordinate: $x = 3$, $y = 1$, and $z = 2$. The local deformation was described by strain tensor E_{ij},

556　　where i and j are the directions of strain and normal plane, respectively. On the other hand, the

557　　stress developed within the area was described by stress tensor P_{ij}, where indices are identical to

558　　those of the strain tensor. These two tensors can be related by the dynamic modulus tensor C_{ijkl},

559　　as $P_{ij} = C_{ijkl} E_{kl}$. Here, P_{ij} is the symmetric tensor and thus, $P_{12} = P_{21}$, $P_{13} = P_{31}$, and $P_{32} = P_{23}$, and

560　　similarly for E_{kl}. Also, $C_{ijkl} = C_{jikl} = C_{ijlk} = C_{klij}$. We also considered transverse isotropy of the

561　　bipolar spindle, where the y-z plane is the isotropic plane, and thus, $C_{55} = C_{44}$ and $C_{22} = C_{11}$ as

562　　Voigt index. Under these assumptions, the longitudinal stress P_{33} can be described as: $P_{33} = C_{13}$

563　　$E_{11} + C_{13} E_{22} + C_{33} E_{33}$. The transverse normal strain we measured experimentally was negligibly

564　　small and therefore, E_{11} and E_{22} were omitted. The longitudinal strain E_{33} was estimated by the

565　　difference in displacements at the peak and edge positions (averaged over values at the two

566　　edges) within the defined 5×5-µm area. On the other hand, the longitudinal stress P_{33} was

567　　defined as the magnitude of force measured by the microneedle probe and the area normal to the

568　　force application vector. The lateral dynamic modulus was estimated under the same assumptions

569　　and was given by $P_{31} = P_{32} = C_{44} E_{31}$.

570

571　　The statistical tests were performed in Origin Pro 9 (Origin Lab Corp) on the basis of two-tailed

572　　Student's t-test.

26

573 **Supplementary information**

574 Supporting data of this manuscript are provided as a separate PDF file. The PDF file includes

575 Supplementary Figures 1–4, and captions of the figures.

576

577 **Acknowledgements**

582

583 **Author contributions**

584 J.T. and Y.S. designed assays, performed experiments, analyzed data, discussed results, and

585 wrote the manuscript.

586

587 **Competing interest statement**

588 The authors declare no competing financial interests.

References

Brugues, J., Nuzzo, V., Mazur, E., and Needleman, D.J. (2012). Nucleation and transport organize microtubules in metaphase spindles. Cell *149*, 554-564.

Burbank, K.S., Groen, A.C., Perlman, Z.E., Fisher, D.S., and Mitchison, T.J. (2006). A new method reveals microtubule minus ends throughout the meiotic spindle. J Cell Biol *175*, 369-375.

Burbank, K.S., Mitchison, T.J., and Fisher, D.S. (2007). Slide-and-cluster models for spindle assembly. Curr Biol *17*, 1373-1383.

Compton, D.A. (1998). Focusing on spindle poles. J Cell Sci *111 (Pt 11)*, 1477-1481.

Desai, A., Murray, A., Mitchison, T.J., and Walczak, C.E. (1999). The use of Xenopus egg extracts to study mitotic spindle assembly and function in vitro. Methods Cell Biol *61*, 385-412.

Dumont, S., and Mitchison, T.J. (2009a). Compression regulates mitotic spindle length by a mechanochemical switch at the poles. Curr Biol *19*, 1086-1095.

Dumont, S., and Mitchison, T.J. (2009b). Force and length in the mitotic spindle. Curr Biol *19*, R749-761.

Elting, M.W., Prakash, M., Udy, D.B., and Dumont, S. (2017). Mapping Load-Bearing in the Mammalian Spindle Reveals Local Kinetochore Fiber Anchorage that Provides Mechanical Isolation and Redundancy. Curr Biol *27*, 2112-2122.e2115.

Gaglio, T., Dionne, M.A., and Compton, D.A. (1997). Mitotic spindle poles are organized by structural and motor proteins in addition to centrosomes. J Cell Biol *138*, 1055-1066.

Ganem, N.J., and Compton, D.A. (2006). Functional roles of poleward microtubule flux during mitosis. Cell Cycle *5*, 481-485.

Garzon-Coral, C., Fantana, H.A., and Howard, J. (2016). A force-generating machinery maintains the spindle at the cell center during mitosis. Science *352*, 1124-1127.

Gennerich, A., Carter, A.P., Reck-Peterson, S.L., and Vale, R.D. (2007). Force-induced bidirectional stepping of cytoplasmic dynein. Cell *131*, 952-965.

Gordon, D.J., Resio, B., and Pellman, D. (2012). Causes and consequences of aneuploidy in cancer. Nat Rev Genet *13*, 189-203.

Goshima, G., Mayer, M., Zhang, N., Stuurman, N., and Vale, R.D. (2008). Augmin: a protein complex required for centrosome-independent microtubule generation within the spindle. J Cell Biol *181*, 421-429.

Hannak, E., and Heald, R. (2006). Investigating mitotic spindle assembly and function in vitro using Xenopus laevis egg extracts. Nat Protoc *1*, 2305-2314.

Hassold, T., and Hunt, P. (2001). To err (meiotically) is human: the genesis of human aneuploidy. Nat Rev Genet *2*, 280-291.

Heald, R., Tournebize, R., Blank, T., Sandaltzopoulos, R., Becker, P., Hyman, A., and Karsenti, E. (1996). Self-organization of microtubules into bipolar spindles around artificial chromosomes in Xenopus egg extracts. Nature *382*, 420-425.

Hiramoto, Y., and Nakano, Y. (1988). Micromanipulation studies of the mitotic apparatus in sand dollar eggs. Cell Motil Cytoskeleton *10*, 172-184.

28

628   Hueschen, C.L., Kenny, S.J., Xu, K., and Dumont, S. (2017). NuMA recruits dynein activity to
629   microtubule minus-ends at mitosis. Elife *6*.

630   Hyman, A., Drechsel, D., Kellogg, D., Salser, S., Sawin, K., Steffen, P., Wordeman, L., and
631   Mitchison, T. (1991). Preparation of modified tubulins. Methods Enzymol *196*, 478-485.

632   Inoue, S., and Salmon, E.D. (1995). Force generation by microtubule assembly/disassembly in
633   mitosis and related movements. Mol Biol Cell *6*, 1619-1640.

634   Itabashi, T., Takagi, J., Shimamoto, Y., Onoe, H., Kuwana, K., Shimoyama, I., Gaetz, J., Kapoor,
635   T.M., and Ishiwata, S. (2009). Probing the mechanical architecture of the vertebrate meiotic
636   spindle. Nat Methods *6*, 167-172.

637   Kapitein, L.C., Peterman, E.J., Kwok, B.H., Kim, J.H., Kapoor, T.M., and Schmidt, C.F. (2005).
638   The bipolar mitotic kinesin Eg5 moves on both microtubules that it crosslinks. Nature *435*, 114-
639   118.

640   Kapoor, T.M., and Mitchison, T.J. (2001). Eg5 is static in bipolar spindles relative to tubulin:
641   evidence for a static spindle matrix. J Cell Biol *154*, 1125-1133.

642   Kashina, A.S., Baskin, R.J., Cole, D.G., Wedaman, K.P., Saxton, W.M., and Scholey, J.M. (1996).
643   A bipolar kinesin. Nature *379*, 270-272.

644   Kwok, B.H., Kapitein, L.C., Kim, J.H., Peterman, E.J., Schmidt, C.F., and Kapoor, T.M. (2006).
645   Allosteric inhibition of kinesin-5 modulates its processive directional motility. Nat Chem Biol *2*,
646   480-485.

647   Mastronarde, D.N., McDonald, K.L., Ding, R., and McIntosh, J.R. (1993). Interpolar spindle
648   microtubules in PTK cells. J Cell Biol *123*, 1475-1489.

649   McIntosh, J.R., Hepler, P.K., and Van Wie, D.G. (1969). Model for mitosis. Nature *224*, 659-663.

650   McKenney, R.J., Vershinin, M., Kunwar, A., Vallee, R.B., and Gross, S.P. (2010). LIS1 and
651   NudE induce a persistent dynein force-producing state. Cell *141*, 304-314.

652   Mitchison, T.J. (2005). Mechanism and function of poleward flux in Xenopus extract meiotic
653   spindles. Philos Trans R Soc Lond B Biol Sci *360*, 623-629.

654   Mitchison, T.J., and Salmon, E.D. (2001). Mitosis: a history of division. Nat Cell Biol *3*, E17-21.

655   Needleman, D.J., Groen, A., Ohi, R., Maresca, T., Mirny, L., and Mitchison, T. (2010). Fast
656   microtubule dynamics in meiotic spindles measured by single molecule imaging: evidence that
657   the spindle environment does not stabilize microtubules. Mol Biol Cell *21*, 323-333.

658   Nicklas, R.B. (1997). How cells get the right chromosomes. Science *275*, 632-637.

659   Oegema, K., and Mitchison, T.J. (1997). Rappaport rules: cleavage furrow induction in animal
660   cells. Proc Natl Acad Sci U S A *94*, 4817-4820.

661   Peter, S.J., and Mofrad, M.R. (2012). Computational modeling of axonal microtubule bundles
662   under tension. Biophys J *102*, 749-757.

663   Redemann, S., Baumgart, J., Lindow, N., Shelley, M., Nazockdast, E., Kratz, A., Prohaska, S.,
664   Brugues, J., Furthauer, S., and Muller-Reichert, T. (2017). C. elegans chromosomes connect to
665   centrosomes by anchoring into the spindle network. Nat Commun *8*, 15288.

666   Salmon, E.D., Leslie, R.J., Saxton, W.M., Karow, M.L., and McIntosh, J.R. (1984). Spindle

667 microtubule dynamics in sea urchin embryos: analysis using a fluorescein-labeled tubulin and
668 measurements of fluorescence redistribution after laser photobleaching. J Cell Biol *99*, 2165-
669 2174.

670 Sawin, K.E., LeGuellec, K., Philippe, M., and Mitchison, T.J. (1992). Mitotic spindle
671 organization by a plus-end-directed microtubule motor. Nature *359*, 540-543.

672 Scholey, J.M., Brust-Mascher, I., and Mogilner, A. (2003). Cell division. Nature *422*, 746-752.

673 Shimamoto, Y., Forth, S., and Kapoor, T.M. (2015). Measuring Pushing and Braking Forces
674 Generated by Ensembles of Kinesin-5 Crosslinking Two Microtubules. Dev Cell *34*, 669-681.

675 Shimamoto, Y., and Kapoor, T.M. (2012). Microneedle-based analysis of the micromechanics of
676 the metaphase spindle assembled in Xenopus laevis egg extracts. Nat Protoc *7*, 959-969.

677 Shimamoto, Y., Maeda, Y.T., Ishiwata, S., Libchaber, A.J., and Kapoor, T.M. (2011). Insights into
678 the micromechanical properties of the metaphase spindle. Cell *145*, 1062-1074.

679 Skibbens, R.V., and Salmon, E.D. (1997). Micromanipulation of chromosomes in mitotic
680 vertebrate tissue cells: tension controls the state of kinetochore movement. Exp Cell Res *235*,
681 314-324.

682 Takagi, J., Itabashi, T., Suzuki, K., Shimamoto, Y., Kapoor, T.M., and Ishiwata, S. (2014).
683 Micromechanics of the vertebrate meiotic spindle examined by stretching along the pole-to-pole
684 axis. Biophys J *106*, 735-740.

685 Tan, R., Foster, P.J., Needleman, D.J., and McKenney, R.J. (2018). Cooperative Accumulation of
686 Dynein-Dynactin at Microtubule Minus-Ends Drives Microtubule Network Reorganization. Dev
687 Cell *44*, 233-247.e234.

688 Torisawa, T., Ichikawa, M., Furuta, A., Saito, K., Oiwa, K., Kojima, H., Toyoshima, Y.Y., and
689 Furuta, K. (2014). Autoinhibition and cooperative activation mechanisms of cytoplasmic dynein.
690 Nat Cell Biol *16*, 1118-1124.

691 Valentine, M.T., Fordyce, P.M., Krzysiak, T.C., Gilbert, S.P., and Block, S.M. (2006). Individual
692 dimers of the mitotic kinesin motor Eg5 step processively and support substantial loads in vitro.
693 Nat Cell Biol *8*, 470-476.

694 Winey, M., Mamay, C.L., O'Toole, E.T., Mastronarde, D.N., Giddings, T.H., Jr., McDonald, K.L.,
695 and McIntosh, J.R. (1995). Three-dimensional ultrastructural analysis of the Saccharomyces
696 cerevisiae mitotic spindle. J Cell Biol *129*, 1601-1615.

697 Yang, G., Cameron, L.A., Maddox, P.S., Salmon, E.D., and Danuser, G. (2008). Regional
698 variation of microtubule flux reveals microtubule organization in the metaphase meiotic spindle.
699 J Cell Biol *182*, 631-639.

700 Yang, G., Houghtaling, B.R., Gaetz, J., Liu, J.Z., Danuser, G., and Kapoor, T.M. (2007).
701 Architectural dynamics of the meiotic spindle revealed by single-fluorophore imaging. Nat Cell
702 Biol *9*, 1233-1242.

703 Zhang, D., and Nicklas, R.B. (1999). Micromanipulation of chromosomes and spindles in insect
704 spermatocytes. Methods Cell Biol *61*, 209-218.

Figure Legends

Figure 1. Microneedle-based setup for analyzing *in-situ* spindle microtubule mechanics.

(**A**) Schematic of the setup. Single metaphase spindles, assembled in *Xenopus* egg extracts and supplemented with X-rhodamine tubulin (20 nM) for microtubule motion tracking, can be subjected to a calibrated force (0.4–1.1 nN) via the microneedle tip (black double arrow). Microtubule motion responses can be analyzed by tracking fluorescent tubulin "speckles" incorporated into the filament lattices (red dots). (**B**) Representative confocal fluorescence image of a spindle, to which a microneedle tip (arrowhead) was inserted and an external force (double arrow) was applied. Yellow rectangle indicates the region for kymograph analysis. (**C, D**) Kymograph generated along the spindle pole-to-pole axis (**C**) and representative speckle trajectories (**D**), showing the motion of tubulin speckles in the absence of an external force. (**E, F**) An externally applied oscillatory force (frequency: 0.1 Hz; amplitude: 0.2 nN) could entrain this motion while maintaining the overall filament dynamics. Roman numbers above each trace correspond to those in the kymographs. Scale bars, 10 μm (horizontal) and 10 s (vertical). (**G**) Amplitude of speckle motion response upon oscillatory force application was determined by sine-wave fitting of each trajectory and mapped onto a single imaging plane. Warmer color indicates larger response amplitude. Black circle with arrowheads, force application position and direction. (**H, I**) Cross-section of the motion amplitude profile along the long (**H**) and short (**I**) spindle axes. Speckle data within dotted rectangles in (**G**) (width: 5 µm) were projected onto each axis. Blue vertical line, spindle equator position.

Figure 2. Microtubule arrays at the middle of the spindle half are less mechanically resistant to force than those near the pole and the equator.

31

728   (**A–C**) Magnitude of speckle motion response depending on position along the long spindle axis,

729   examined using an oscillatory force (0.1 Hz) applied near the spindle pole (**A**), at the middle of

730   the spindle half (**B**), and near the equator (**C**). Data from multiple spindles (grey lines, n = 5

731   each) were each aligned at baseline, pooled and averaged at 1 µm bin width (navy plots). Bars

732   are S.D. Vertical bars in light blue, approximate equatorial position. (**D**) The averaged profiles in

733   (**A–C**) were each normalized to the peak value and overlaid at the peak position. (**E–G**) The data

734   in (**A–C**) were analyzed for speckles that located along the short spindle axis. (**H**) Normalized

735   amplitude profiles of (**E–G**) generated as in (**D**). (**I**) Local effective stiffness at each spindle

736   region, as estimated on the basis of each motion amplitude profile within ±5 µm from the peak

737   (grey highlighted area in (**A–C**) and (**E–G**)). Data are mean ± SD (n = 5 each). *p <0.05

738   **p<0.01, two-tailed Student's t-test. N.S., not significant. (**J, K**) Local mechanical properties of

739   the spindle, measured by microrheology (see Fig. S2). Oscillatory forces were applied along the

740   long spindle axis and at varied frequency (0.01–4 Hz) (n = 10 at each spindle location). Dynamic

741   stiffness (**J**) represents total mechanical resistance associated with viscous and elastic

742   deformations. Phase shift (**K**) is a measure of how elastically ($\theta = 0$) or viscously ($\theta = \pi/2$ rad)

743   the structure is deformed.

744

745   **Figure 3. Local mechanical responses of spindle microtubules are independent of filament**

746   **polarity.**

747   (**A**) Two-dimensional heat maps showing the dependency of speckle motion amplitude on

748   microtubule polarity. Speckles that had been moving toward the left and right spindle poles

749   (tracked over ≥10 s) are analyzed for directionality and mapped in separate panels. Black circle,

750   force application location (frequency: 0.1 Hz; amplitude: 0.25 nN). Warmer color indicates larger

32

751   amplitude response. Open circles in each map are the fraction of speckles that were assigned the

752   opposite polarity. (**B**) Ratio of leftward- versus rightward-moving speckles (black squares and

753   red circles, respectively) as a function of the position along the long spindle axis. Data from n =

754   4 spindle samples were pooled and averaged at each 5-µm bin. Bars are SDs. (**C**) Individual

755   speckle motion amplitude in (**A**) is projected along the long spindle axis. Speckles moving

756   toward the left and right spindle poles are plotted in different symbols (blue squares and red

757   circles, respectively). Other marks are as in Fig. 1. (**D**) Averaged motion amplitude of leftward-

758   and rightward-moving speckles at different spindle location, obtained from n = 4 spindles. Data

759   as in (**C**) are pooled and averaged at each 5-µm bin. Bars are SDs.

760

761   **Figure 4. Spindle length change is coupled with sliding of microtubule arrays nearer the**

762   **pole.**

763   (**A**) Dual microneedle-based setup for examining microtubule motion dynamics associated with

764   spindle length change. Microtubules were double-labeled with X-rhodamine-tubulin (red, 20

765   nM) and Alexa 488-tubulin (green, 400 nM) for speckle imaging and spindle length

766   measurement, respectively. One microneedle (M1) is used to pin down the spindle while the

767   other (M2) can be moved at 100 nm/s to apply outward stretching force. (**B**) Confocal snapshots

768   of a spindle before and during the course of a stretch. Merged images of labeled tubulins (red: X-

769   rhodamine; green: Alexa 488) are shown. Chromosomes were also labeled with SYTOX green

770   dye. Dotted lines indicate changes in microneedle tip positions. Scale bar, 10 μm. (**C**)

771   Kymograph generated along the spindle pole-to-pole axis in (**B**) (line width: 3 µm). Arrowheads,

772   initial microneedle tip positions. Following the onset of microneedle movement ($t = 0$), the

773   spindle first underwent a brief period of parallel translocation (0–25 s, labeled "Trans") and was

33

774 then stretched at a nearly constant velocity (25–135 s, labeled "Stretch"). Horizontal scale bar, 10

775 μm; vertical scale bar, 20 s. (**D**) Time course of spindle-length change. Orange highlighted area

776 indicates the period over which the spindle was stretched. Slope is 94 nm/s ($R^2 = 0.98$) by linear

777 regression. The following analyses were performed at the highlighted steady stretching phase.

778 (**E**) Speckle motion response. Trajectories of individual speckles that could be tracked for ≥10 s

779 were projected onto a single imaging plane. Grey ovals with broken and solid lines are

780 approximate spindle positions at the onset and the end of stretch, respectively. (**F–I**) Speckle

781 velocity analyzed before stretch (**F, G**) and during steady stretching phase (**H, I**). Heat maps (**F,**

782 **H**) were generated on the basis of the average velocity of individual tubulin speckles relative to

783 spindle center and plotted at their initial position along the spindle axes. (**G, I**) Dependence of

784 speckle velocity on the position along the long spindle axis. Histograms indicate overall velocity

785 distribution of all the speckles analyzed. (**J**) Magnitude of the increase in average speckle

786 velocity upon application of a stretching force as a function of the long-axis spindle position.

787 Data obtained from n = 4 spindles were pooled and averaged at every 0.1 relative spindle

788 position bin. Grey lines are trends predicted from a simple multifilament array model (**K**) (see

789 also Fig. S3C), which assumes that the predominant relative filament movement occurred evenly

790 across the spindle (broken line), near the pole (solid line), or near the equator (dotted line).

791

792 **Figure 5. Effect of motor protein inhibition on the local mechanical responses of**

793 **microtubules.**

794 Results of molecular perturbation assays with 1.5 mM AMPPNP (n = 3) (**A–E**), 10 μM or 20 μM

795 monastrol (n = 3 and 5) (**F–J**), and 1 mg/ml anti-dynein 70.1 antibody (n = 4) (**K–O**). (**A, F, K**)

796 Representative confocal snapshots of spindles upon drug treatment. Local microtubule responses

34

797   were measured using an oscillatory force (0.1 Hz) at various spindle locations (indicated by

798   white dotted lines). Average motion amplitude profiles were then generated along the long

799   spindle axis measured near the spindle pole (**B, G, L**), at the middle of the spindle half (**C, H, M**),

800   and at the equator (**D, I, N**). Averaged profiles from non-treated spindles are shown for

801   comparison (black, corresponding to Fig. 2). (**E, J, O**) Local dynamic moduli were estimated on

802   the basis of force and deformation magnitude within the ±5-µm area in each profile (grey). Data

803   are mean ± SD. All scale bars are 10 μm. *p <0.05, **p<0.01, two-tailed Student's *t*-test. N.S.,

804   not significant.

805

806   **Figure 6. Model for the local mechanical architecture of the spindle.**

807   (**A**) Schematic of the metaphase spindle. Open circles, microtubule minus-ends. Short

808   antiparallel microtubules assemble near the equator, while parallel microtubules predominate

809   nearer the pole. The ends of the equatorial and polar microtubule arrays overlap at the middle of

810   the spindle half (highlighted in blue) and form parallel filament arrays, adapting to force

811   associated with spindle-length change (dotted lines). The arrays at the pole and the equator are

812   mechanically more robust and maintain their steady-state architecture against perturbing force

813   (highlighted in orange). (**B**) Schematic of the molecular interactions involved in spindle

814   micromechanics. Kinesin-5 (orange) localizes across spindle microtubules, pushing and resisting

815   filament sliding to maintain the pole and equatorial dynamics, while its contribution to filament

816   crosslinking at the middle of the spindle half is relatively small. Dynein (blue) localizes at the

817   minus-ends of microtubules and mediates parallel filament interactions at the spindle pole and
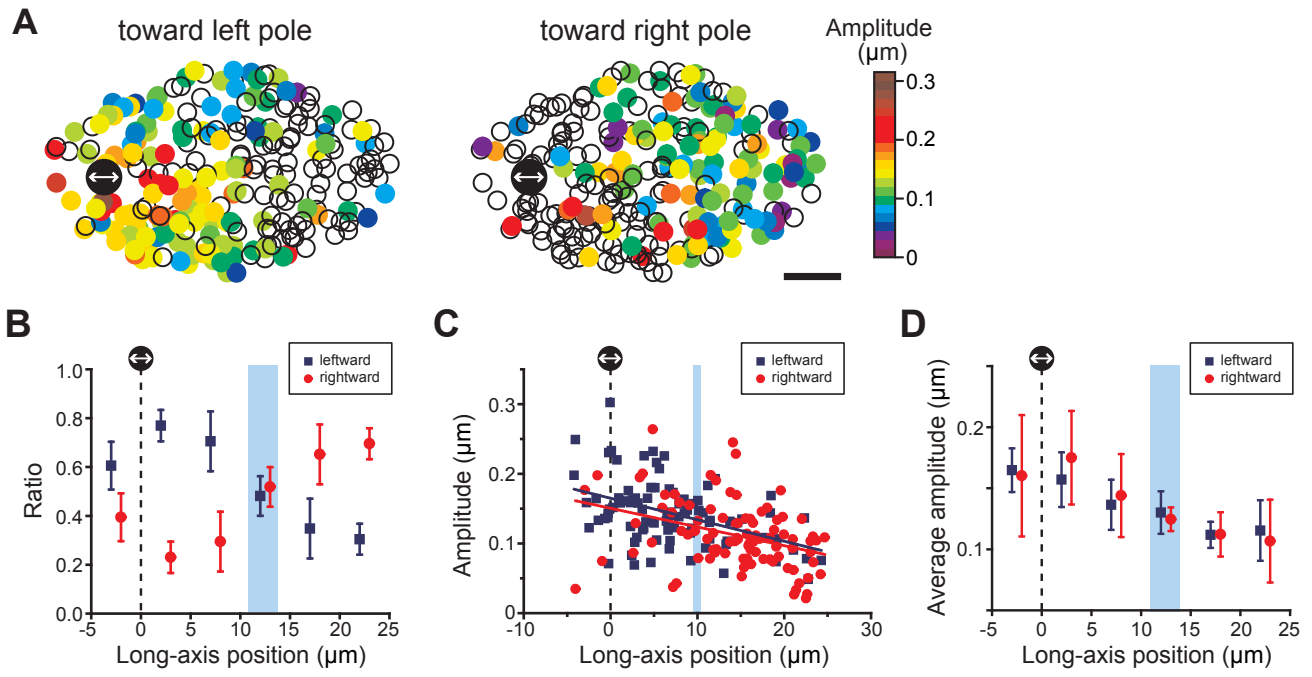
818   middle of the spindle half.
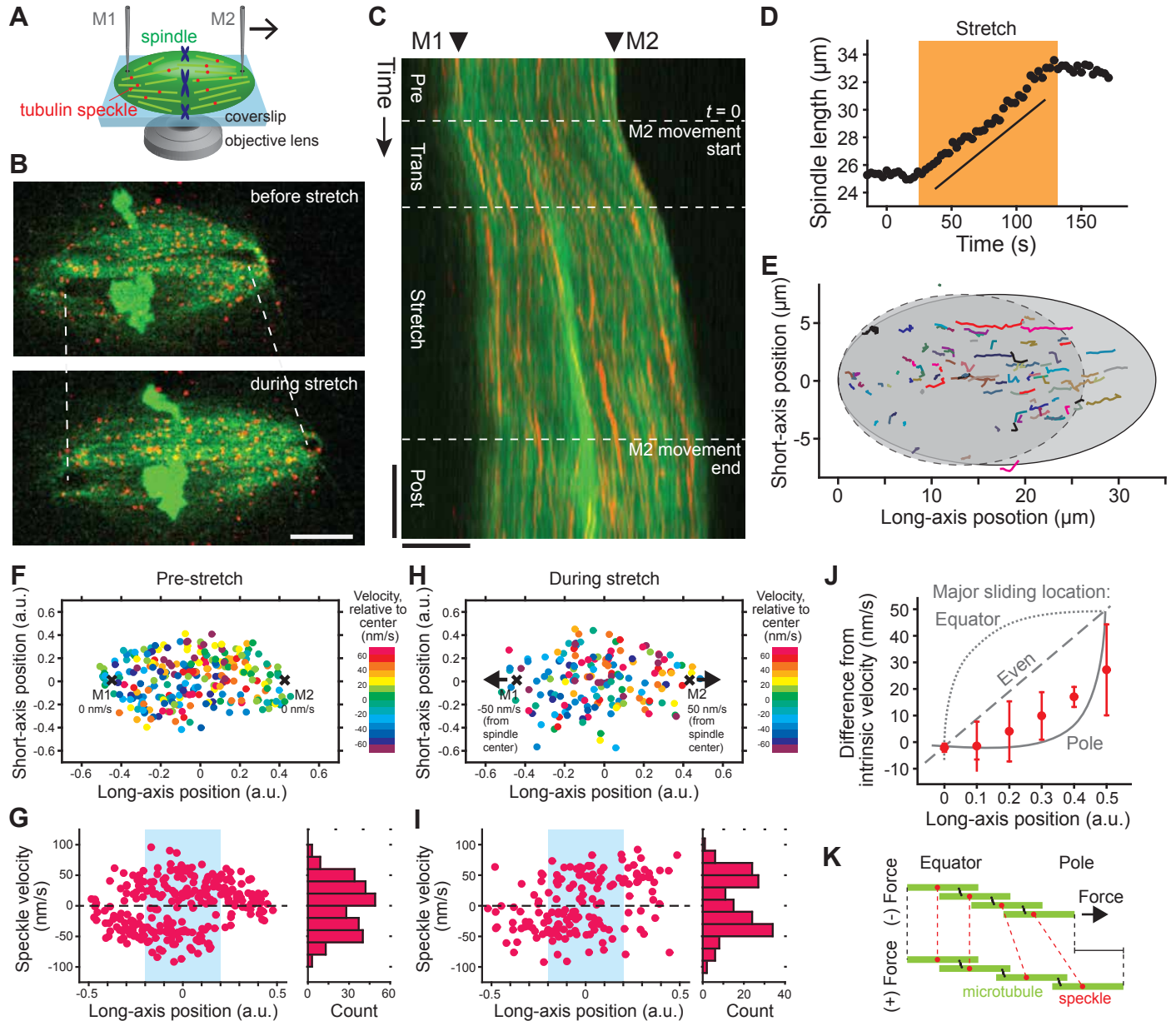
819

35

Takagi and Shimamoto, Figure 1
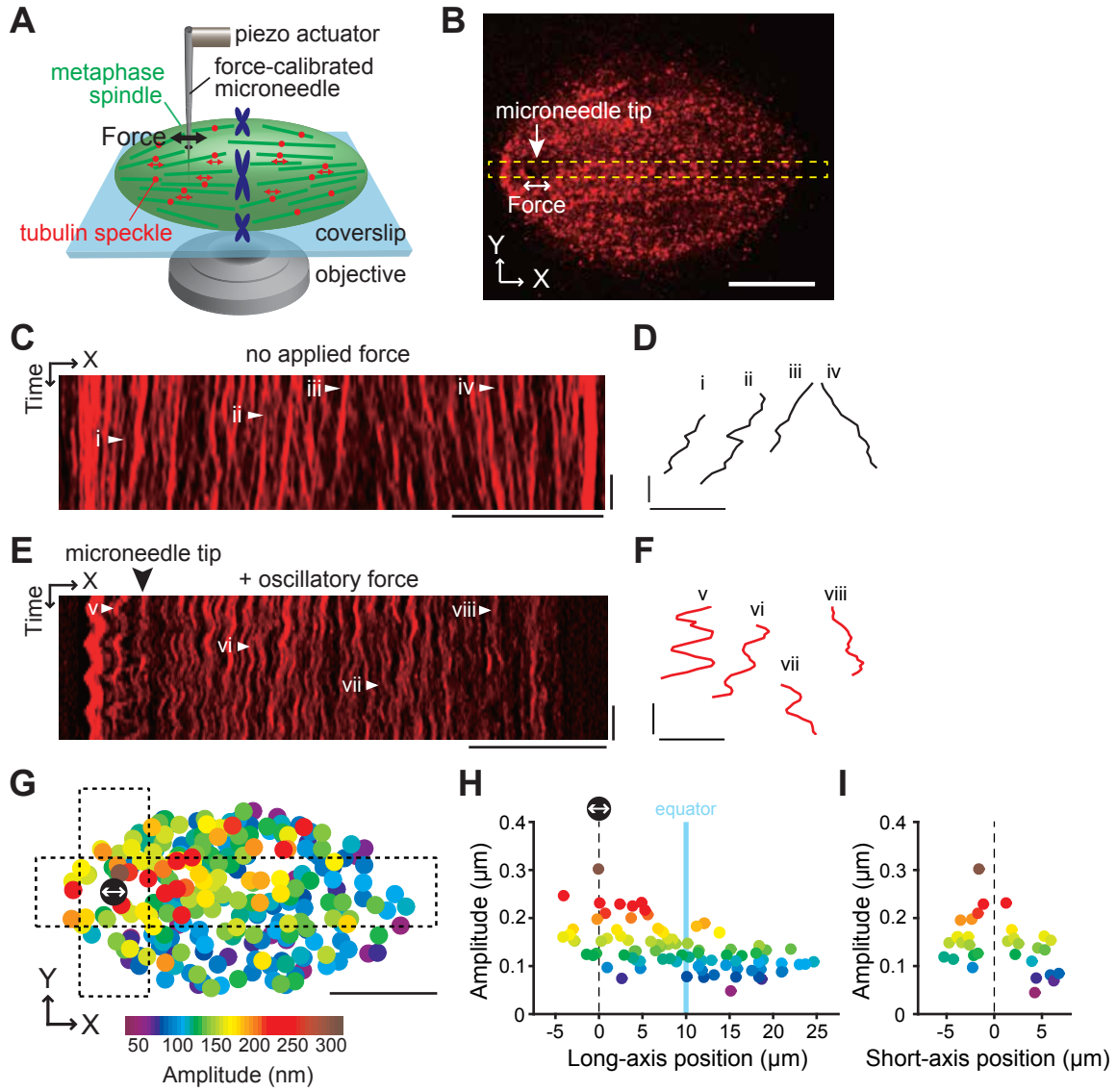
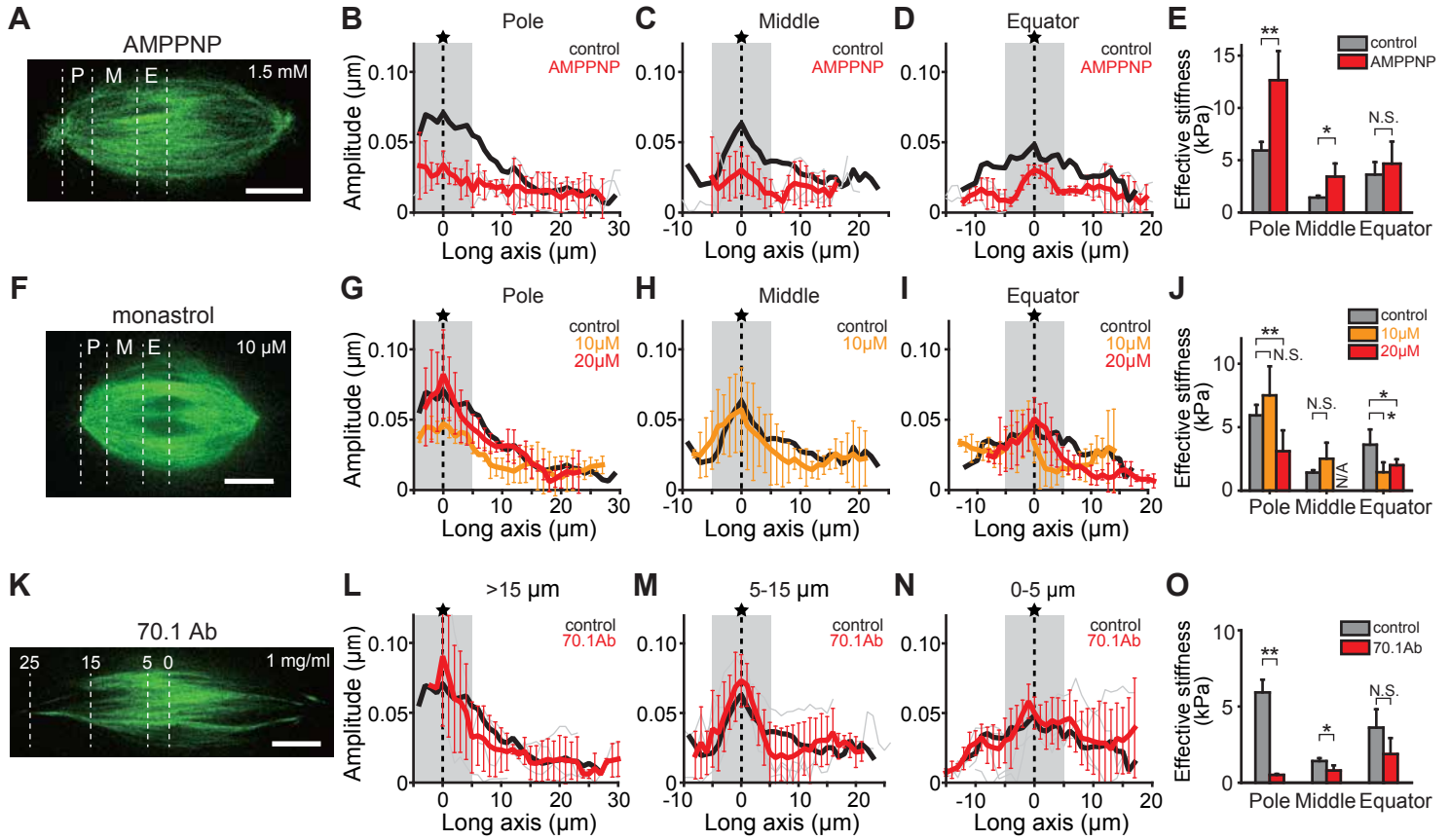Takagi and Shimamoto, Figure 2
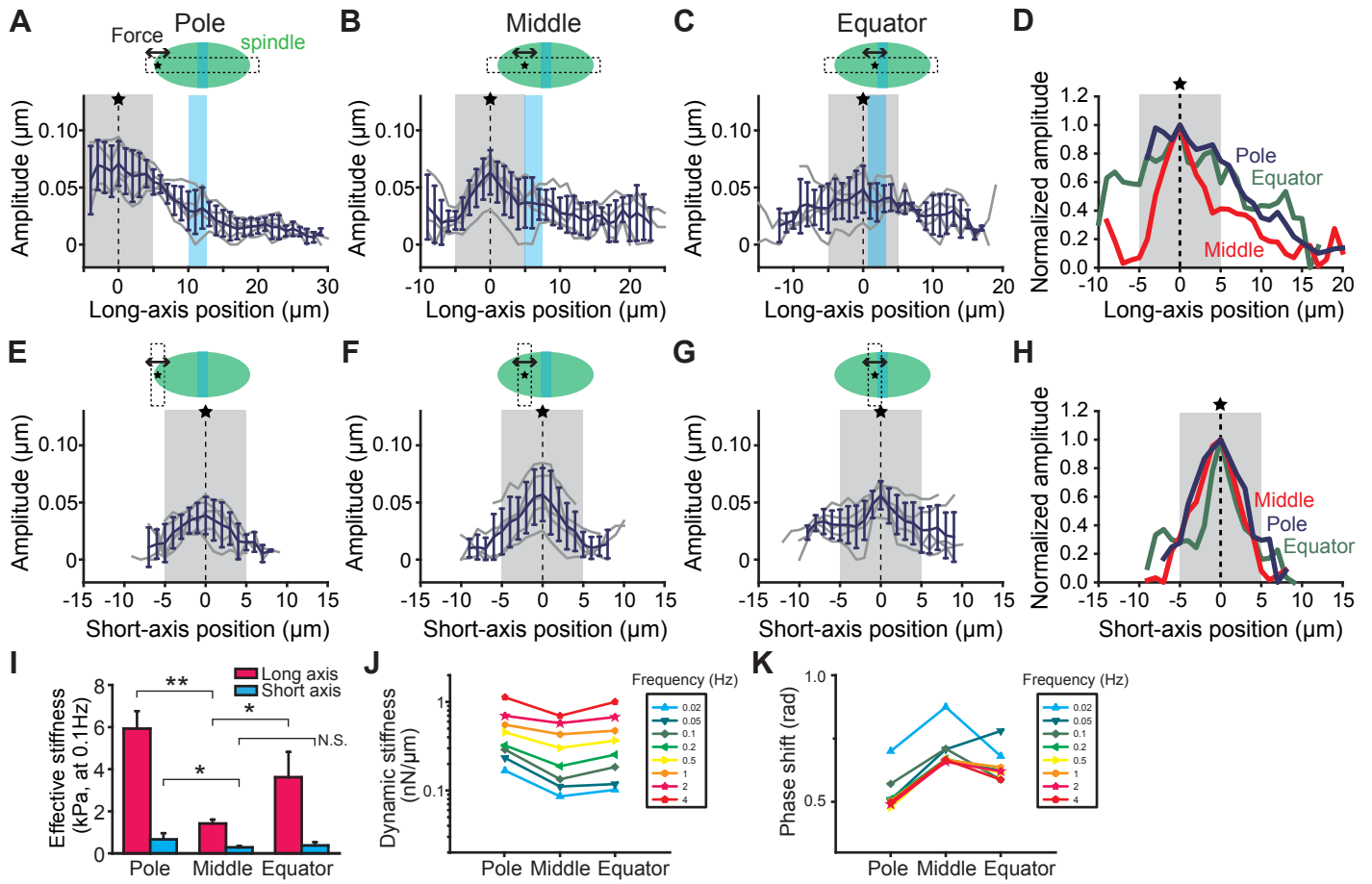
Takagi and Shimamoto, Figure 3

Takagi and Shimamoto, Figure 4

Takagi and Shimamoto, Figure 5

Takagi and Shimamoto, Figure 6

A Metaphase spindle

B

	Pole	Middle	Equator
architecture:	Parallel	Parallel	Antiparallel
rigidity:	Rigid	Soft	Rigid
viscoelasticity:	Elastic	Viscous	Viscous
motor (function):	kinesin-5 dynein (cluster)	dynein (slide)	kinesin-5 (push/brake)